ELSEVIER

Contents lists available at ScienceDirect

# Scripta Materialia

journal homepage: www.journals.elsevier.com/scripta-materialia





# Surface oxide layer strengthening and fracture during flattening of powder particles

Qi Tang <sup>a</sup>, Yuji Ichikawa <sup>b,\*</sup>, Mostafa Hassani <sup>a,c,\*</sup>

- <sup>a</sup> Sibley School of Mechanical and Aerospace Engineering, Cornell University, Ithaca, NY 14853, USA
- <sup>b</sup> Fracture and Reliability Research Institute, Tohoku University, Sendai, 980-8579, Japan
- <sup>c</sup> Department of Materials Science and Engineering, Cornell University, Ithaca, NY 14853, USA

## ARTICLE INFO

#### Keywords: Surface oxide layer Particle compression Fracture Composite strengthening Strain gradient

### ABSTRACT

Surface oxide layer fracture and the subsequent exposure of clean metallic surfaces are critical in various solidstate processes for powder consolidation and additive manufacturing. We resolve this process *in-situ* by deforming individual spherical powder particles inside a scanning electron microscope. We reveal three fracture modalities, i.e., meridian, radial, and circumferential cracking that sequentially activate with particle flattening. Real time measurements of load and displacement upon particle flattening also reveal a significant strengthening effect by surface oxide. We attribute the strengthening to two mechanisms: the composite strengthening and the strain gradient strengthening.

Metallic powder particles are often covered with a native oxide layer on their surfaces. Understanding the fracture behavior of the oxide layer and its effect on the deformation behavior of the particles is essential in many solid-state processes from cold spray additive manufacturing [1–9] to ultrasonic powder compaction [10,11] and friction stir powder consolidation [12–14]. A central mechanism in all these processes is the deformation-induced fracture of the surface oxide layer and the subsequent exposure of the underlying fresh metallic surfaces to achieve metallurgical bonding upon intimate contact [9,15–26]. Despite its pivotal role, mechanistic discussions around oxide layer fracture at a single powder particle level remains mostly phenomenological [27–30] or simulation-based [31–34] because the small length-scales involved, i. e.,  $\sim \! 10 \; \mu m$  for powder particles and  $\sim \! 10 \; nm$  for oxide layers make real time observations challenging.

In this work we aim to address the above challenge using *in-situ* observations of oxide layer fracture and instrumented measurements of the load and displacement upon flattening of individual powder particles. We flattened spherical metallic particles with and without a surface oxide layer inside a scanning electron microscope (SEM) while recording oxide layer cracking in real time. We also measured the strengthening effect of the surface oxide layer and discussed it in light of the superposition of the composite and the strain gradient effect. We conducted finite element (FE) simulations to support our experimental findings.

Gas atomized polycrystalline Aluminum (Al) particles (THP-A20S,

Toyo Aluminum K.K., Osaka, Japan) were annealed in a vacuum furnace at 200 °C for 3 h to produce single crystal Al particles (see cross-sectional micrographs in the supplementary material). Using barrel sputtering (Toshima Manufacturing Co., Ltd., Saitama Japan), ZnO was then coated on particles surface. Process conditions were controlled to achieve a uniform oxide layer thickness of  $\sim$ 30 nm (see supplementary Figure S1). The choice of ZnO was intentional to achieve a chemical contrast between the oxide layer and the underlying Al that enables resolving oxide layer fracture upon particle flattening. For the gas atomized particles with and without ZnO layer, we expect a ~5 nm thick native oxide layer attached to the surface [15]. However, given the commonality of the native oxide layer in both cases, any experimentally measured or observed differences can be attributed to the ZnO oxide layer. Particle compression tests were conducted on particles with and without an oxide layer inside a LEO 1550 SEM using a micromechanical testing stage (Alemnis AG, Switzerland) and a 50- $\mu$ m-diameter flat punch diamond tip (Fig 1a). The particles were selected to have an average diameter of  $10 \pm 0.5 \, \mu m$  to exclude any possible size effect. The particles were compressed against a rigid sapphire plate. Particle compression was conducted under a constant loading rate of 1.334 mN/s until a displacement of 5  $\mu m$ , resulting in a nominal strain of  $\sim 70$  % (see the supplementary video). Nominal strain is defined as [35]:

$$\varepsilon_{nom} = -\ln\left(1 - \frac{\delta}{d_0}\right) \tag{1}$$

E-mail addresses: ichikawa@tohoku.ac.jp (Y. Ichikawa), hassani@cornell.edu (M. Hassani).

https://doi.org/10.1016/j.scriptamat.2024.116008

Received 18 September 2023; Received in revised form 13 December 2023; Accepted 25 January 2024 Available online 2 February 2024

<sup>\*</sup> Corresponding authors.

Q. Tang et al. Scripta Materialia 244 (2024) 116008

where  $\delta$  is the displacement and  $d_0$  is the initial particle diameter. The load-displacement data was continuously recorded for all particles. In addition, interrupted compression tests were conducted on particles with surface oxide layer to reveal possible oxide fracture modalities. In the interrupted compression tests, particles were compressed in multiple 1- $\mu$ m compression steps, until a nominal strain of 200 %. The tip was retracted after each intermediate step so that the deformed particle and the evolution of the oxide layer fracture can be imaged.

Fig. 1b shows a single crystal Al particle before and after compressing to a nominal strain of 65 %. While the surface of the particle is smooth before the deformation, we can observe the appearance of slip bands (dashed lines) after the deformation. The double-slip behavior in Fig 1b is a characteristic of stage II hardening, where the interaction of dislocations in nonparallel planes and strong work hardening is expected [36, 37]. Fig. 1c shows the deformation of the Al particle with oxide layer to similar flattening level. The oxide layer exhibits no sign of defects or cracks before the deformation. However, significant cracking can be observed for the flattened particle on the side and the top surfaces. The side surface is fractured primarily through meridian cracks (white arrows). We also observe inclined meridian-like cracks in the particle with oxide oriented similarly to the slip bands observed for the particle with no surface oxide. The slip steps introduced an out-of-plane shear force and affected the propagation orientation of the meridian cracks. The darker-shaded regions within the gaps created by these cracks indicate the exposure of the underlying metallic surfaces.

The snapshots shown in Fig. 1d were captured during the interrupted particle compression test conducted specifically to reveal the sequence of oxide layer cracking events. We observe no cracks after the first 1- $\mu m$  compression despite a nominal strain of 15 %. The first fracture modality appears in the 15–28 % strain range involves meridian cracks. The opening appears to be largest at the center suggesting that the meridian cracks initiate at the particle's "equator" and propagate towards the top and bottom edges. We observe a second fracture modality at 39 % nominal strain (Fig. 1e). Here, the meridian cracks extend to the top surface and form radial cracks. As the compression continues the opening of the meridian cracks increases and the radial cracks propagate towards the center. We observe the third fracture modality at even larger

strains; circumferential cracks form in between the radial cracks on the top surface (Fig. 1f). These fracture modalities are schematically summarized in Fig. 1g.

Fig. 2a shows the load as a function of displacement for particles with and without oxide. The load is averaged over three repetitive tests, and the standard deviation is represented by the shadow around the solid line. While differences in crystal orientation are anticipated for the tested single crystal Al particles, it is interesting to note that the loaddisplacement data for several tested particles (Fig. 2a) shows a relatively small standard deviation of 10 % (with oxide) and 4 % (without oxide). In contrast to the significant impact of orientation observed in uniaxial loading [38,39], in the processes that introduce multi-axial stress state, the effect of orientation on single crystal deformation is less significant [40]. What is more, the activation of multiple slips systems under very large strains further contribute to small variations in the measured load displacement data from one particle to another. Following the approach proposed by Assadi et al. [35], we map the load displacement data to the particle level stress and strain using Eqs. (1) and (2) with F being the compressive load. We highlight that the mapping is not to suggest a uniaxial stress state for particles. It is rather to associate a characteristic stress and strain with which both the size and the continuously increasing contact area effects can be excluded from

$$\sigma_{nom} = \frac{4F}{\pi d_0^2} \frac{d_0 - \delta}{d_0} \tag{2}$$

Fig. 2b shows the particle level stress and the work hardening rate as a function of the particle level strain. Considering that the Peierls stress is very small for single crystal Al (on the order of  $\sim 1$  MPa [36,41–44]), we can identify the initial nearly linear part of the stress strain curve for the particle with no oxide as a representation of stage II hardening. In this stage, dislocation slip occurs in more than one set of planes (see Fig. 1b). Our results show a relatively small stage II tansitioning to stage III hardening at around 9 MPa. This is expected in metals with high stacking fault energies such as Al as they can deform so easily by cross slip. The rest of the deformation in stage III occurs with a gradually decreasing hardening rate indicating the increasing role of dynamic

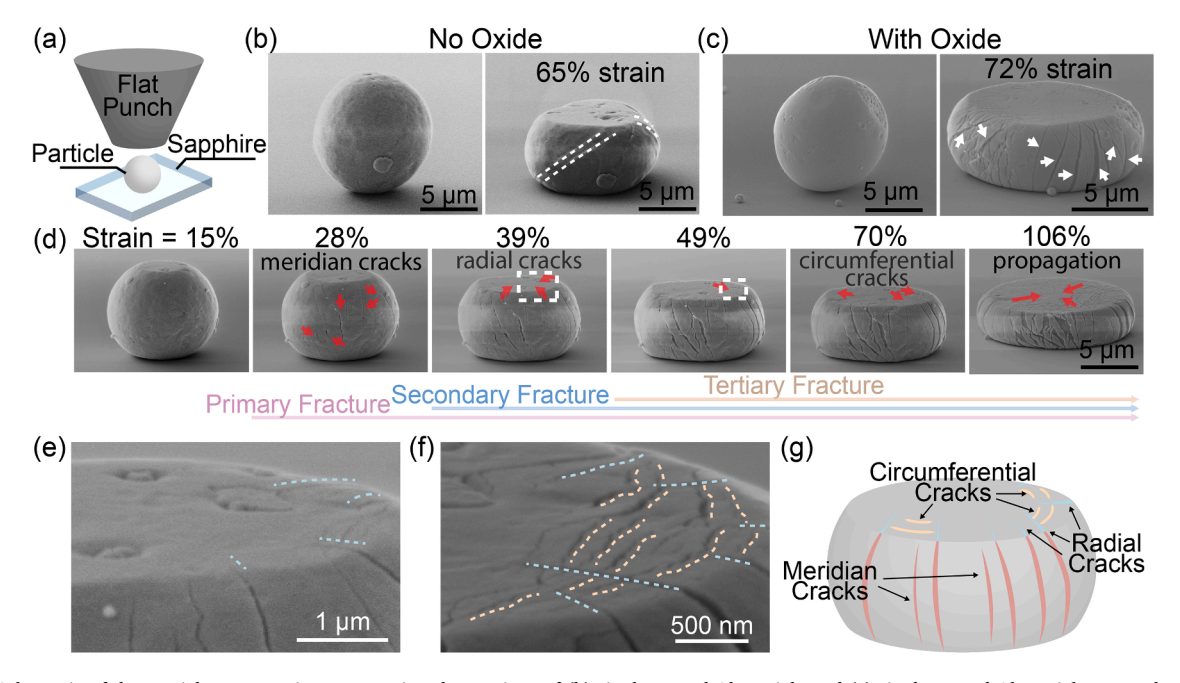


Fig. 1. (a) Schematic of the particle compression test. In-situ observations of (b) single-crystal Al particle and (c) single crystal Al particle covered with a surface oxide layer before and after flattening. (d) Interrupted compression test of an Al particle with surface oxide layer shows the evolution of the oxide layer fracture and different cracking modalities. Closer views of the oxide layer fracture on the top surface, at nominal strains of (e) 39 % and (f) 49 %. (g) Schematic representation of the oxide layer fracture modalities.

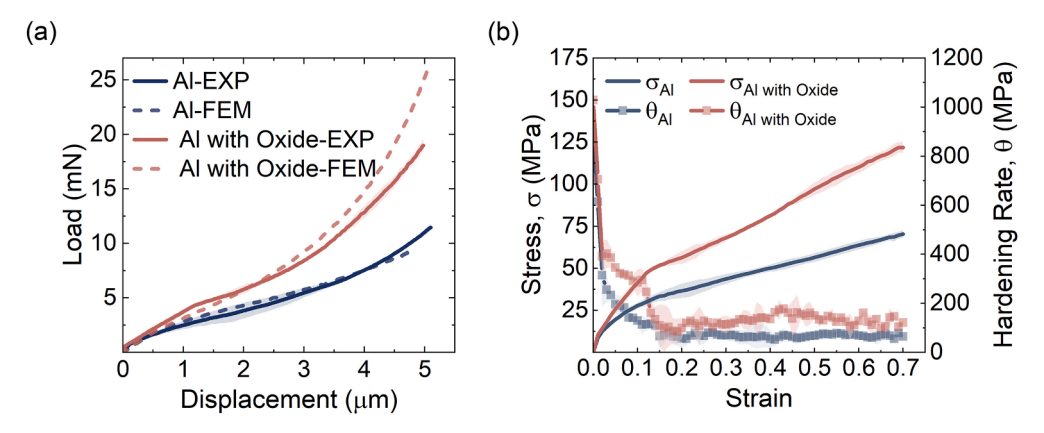


Fig. 2. (a) Experimental measurements and numerical predictions of the load-displacement behavior for particles with and without surface oxide. (b) Nominal stress-strain curves mapped from the load-displacement data and the corresponding work hardening rates as a function of the particle level strain.

recovery processes.

The nominal stress-strain behavior of the particle with oxide shows interesting contrasts with the bare particle. First, the oxide layer brings about considerable strengthening effect. The transition from stage II to stage III hardening occurs at a higher level of stress, 14 MPa, and the stress required to flatten the particle to 70 % strain is increased by a factor of 1.75. While the strengthening is expected with the presence of the oxide layer, its level is somewhat surprising especially when considering that oxide layer comprises only a  $\sim$ 1.8 % volume fraction of the entire particle. Second, we observe a higher work hardening rate for the particles with oxide layer at strains below  $\sim 12$  %, before oxide layer fracture initiates. We can attribute this extra hardening to the composite strengthening effect. Third, we observe a significant drop in the rate of work hardening for particles with oxide layer in strains ranging from  $\sim$ 12 % to  $\sim$ 20 %. This regime coincides well with the occurrence of significant cracking activities observed in our in-situ interrupted compression test and therefore can be attributed to the oxide layer fracture. Fourth, we observe a slight increase in the work hardening rate of the particles with oxide starting at  $\sim$ 20–25 % strain range after which the work hardening rate remains higher than the bare particle for the remainder of the deformation.

To better understand the oxide layer fracture as well as its strengthening effect, we conducted 2D axisymmetric FE simulations of the flattening of 10-µm Al particles with and without a 30-nm ZnO oxide layer (See supplementary material for the simulation details and Fig. 2a for the predicted load-displacement data). Distributions of the circumferential and radial components of stress within the oxide layer are shown in Fig. 3 for different particle-level strains. As the particle flattens, the circumferential stress increases with a higher rate compared to the radial stress. This explains why meridian cracks are the first fracture modality observed in the experiment. Our simulation shows that in the strain range of 15–28 % where meridian cracks occur during the

experiment, the circumferential stress on the side surface is 4-6 GPa. This stress level corresponds well with the fracture strength reported for ZnO at small scales, ranging from 2 to 8 GPa [45,46]. The peak circumferential stress is located at the "equator" of the particle where we identified as the region where meridian cracks initiated in the experiment.

As the particle further flattens, the circumferential stress on the top surface also increases. At 39 % strain it reaches the fracture threshold level,  $\sim$ 4–6 GPa, at the edge on the top surface. This is also in accord with the strain level at which the radial cracks on the top surface were observed. With even further flattening of the particle, the radial stress on the top surface also approaches the threshold for fracture and drives the formation of the circumferential cracks in between the radial cracks. Our results also show that both stress components remain relatively low (less than 2 GPa) in the central area on the top surface. This aligns with the observation of no significant cracking activities in this region at 70 % strain.

To understand the significant oxide layer strengthening we first examine the composite effect:

$$\sigma_{Composite} = (1 - f)\alpha\sigma_{Al} + f\alpha\sigma_{Oxide}$$
(3)

where f is the volume fractions of the oxide layer,  $\sigma_{Al}$  and  $\sigma_{Oxide}$  are the average nominal stresses carried by the Al particle and the oxide layer respectively, and  $\alpha=0.8$  is a correction factor to account for the deviation from the isostrain condition (see supplementary material). The strengthening defined as the difference between the particle level stresses with and without the oxide layer can be approximated as:

$$\Delta \sigma = \sigma_{Composite} - \sigma_{Al} \tag{4}$$

Fig. 4 compares the overall strengthening measured experimentally with the composite strengthening predicted from Eq. (4). We used the

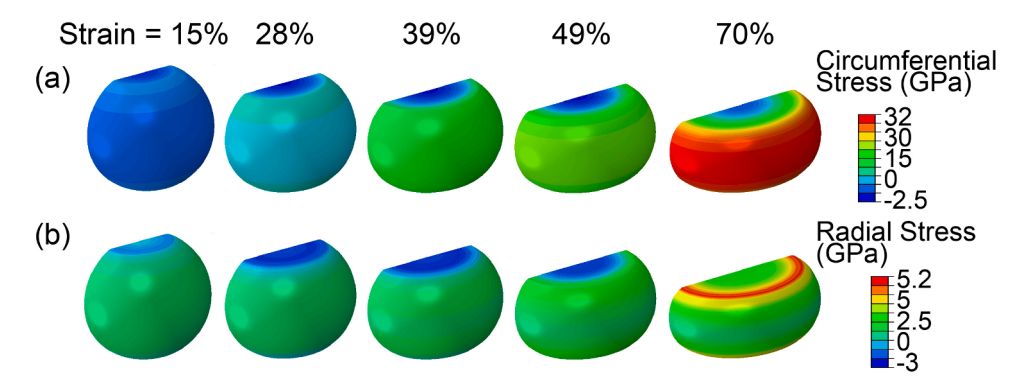


Fig. 3. Distribution of (a) circumferential and (b) radial components of stress within the 30-nm surface oxide layer at various strain levels.

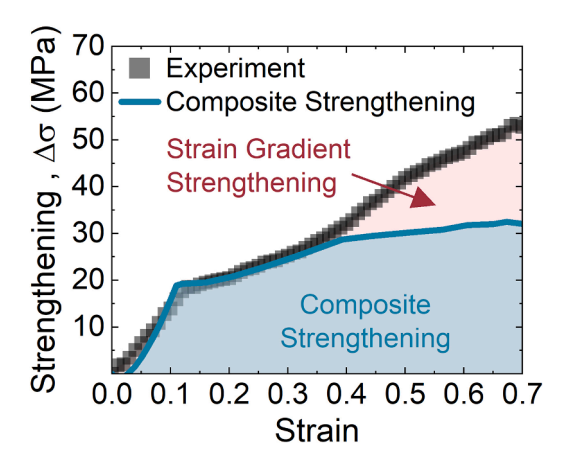


Fig. 4. Strengthening measured from experiment compared to the ones estimated from the composite effect.

nominal stress in Al from Al particle compression experiments and the volume averaged Mises stress in the oxide layer from our FE simulations. In constructing the plot, we assumed that the average stress of the oxide layer reaches an upper bound on the side surface as well as on the top/ bottom surfaces when meridian and radial cracks form respectively. In the early stage of flattening, the good agreement between the experimental measurements and the prediction shows that composite effect is indeed the strengthening mechanism during this stage. We observe a reduction in the strengthening rate at  $\sim$ 12 % strain which we attribute to oxide layer fracture. Nevertheless, the two curves still closely follow each other up to  $\sim 30$  % strain. This confirms the assumption that after cracking on the side surface, it is the oxide layers on the top and bottom surfaces that continue the composite strengthening. We notice a deviation between the two curves starting at the strain range of 20-30 %. The deviation becomes larger as the particle flattens further. With significant cracking relaxing the stress in the oxide layer, especially at larger strains, it is not physically plausible for the oxide layer to be able to accommodate the increasing rate of strengthening observed at later stages of flattening. The increasing gap between the two curves suggests that an additional strengthening mechanism should be operative toward the end.

To identify the additional strengthening mechanism, we closely examine the evolution of the equivalent plastic strain in Al particles with and without oxide in Fig. 5a. At the early stage we observe the formation of a plastic "backbone" in which the majority of the material flow occurs through the inward pushing of the top and bottom plastic zones (white arrows) [47–49]. The most highly strained regions are located on the surfaces in contact with the punch/substrate at this stage. As further

flattening continues, a major strain redistribution occurs with a shift in the location of the highest plastic strain from the top/bottom surfaces to the plastic core. The formation of a highly strained core occurs at  $\sim\!25\,\%$  and  $\sim\!30\,\%$  for the particles with and without oxide respectively. As the core region gets harder with the accumulation of plastic strain, the flattening of the particle is mainly accommodated by a lateral plastic flow (yellow arrows). In the particle with oxide, we observe an earlier formation of the highly deformed core and a higher strain gradient. Geometrically necessary dislocation (GND) are required to accommodate the strain gradient from the top surface to the core. While GNDs strengthen both particles, our results suggest the degree of strengthening is greater for the particle with oxide compared with the bare particle. On this basis we propose strain gradient strengthening to be the additional strengthening mechanism.

To show that strain gradient hardening can indeed cover the gap between the measured strengthening and the composite effect in Fig 4, we approximate, to the first order, the strain gradient contribution to strengthening by  $\Delta \sigma_{GND} \approx \alpha \mu b (\sqrt{\rho_{GND,composite}} - \sqrt{\rho_{GND,Al}})$ . Here  $\mu$  is shear modulus,  $\alpha = 0.5$  is a constant, and b is the magnitude of Burgers vector. The density of GNDs can be estimated as  $\rho_{GND}=\eta/b$  with  $\eta$  being the plastic strain gradient [50]. We estimate the plastic strain gradient along the axis of symmetry as the difference between the plastic strain at the core and the plastic strain on the surface divided by the particle diameter. The strains are taken from the FE simulations. We estimate the strain gradient contribution to strengthening at 50 % and 70 % strain to be 18 MPa and 31 MPa respectively. These values are close to the gap between the measured strengthening and the composite effect, i.e., 15 MPa at 50 % strain and 20.7 MPa at 70 %. This analysis further supports the role of strain gradient as the additional strengthening mechanism in particle flattening. While the strain gradient is negligible up to a strain of 20~30 %, before the formation of the highly deformed particle core, it plays an increasing role at the later stages of the flattening.

Fig. 5b shows the FE predictions of the strain gradient as a function of the Al particle surface area-to-volume ratio and the oxide thickness-to-Al particle diameter ratio. The map was specifically constructed for a 40 % strain in the Al particles at which level all the particles have already developed a highly deformed core. The map illustrates that the strain gradient level is predominantly influenced by the surface area-to-volume ratio. When comparing particles with oxide to bare particles at a constant surface area-to-volume ratio, there is a substantial increase in the strain gradient. However, once an oxide layer forms, further thickening of the oxide layer only leads to a marginal rise in the strain gradient.

In summary, we resolve, in real time, the fracture of surface oxide layer upon flattening of powder particles. We found that oxide layer fracture occurs with three cracking modalities. It starts with meridian cracks on the side surface. As the particle further flattens, radial cracking

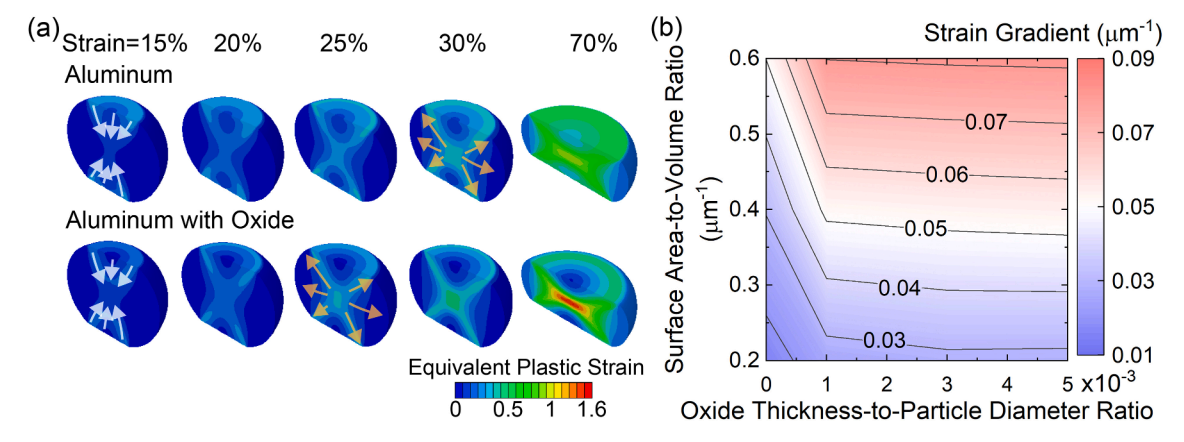


Fig. 5. (a) Distribution and evolution of the equivalent plastic strain for Al particles with and without oxide. (b) Strain gradient map as a function of surface area-to-volume ratio and oxide thickness-to-particle diameter ratio at a fixed strain of 40 %.

Q. Tang et al. Scripta Materialia 244 (2024) 116008

and eventually circumferential cracking appear on the top (and bottom) surfaces. FE simulations suggest that this specific sequence is driven by the distribution and the evolution of the circumferential and radial components of stress. The combination of these three cracking modalities provide an efficient mechanism to expose the underlying fresh metallic surfaces. We also report significant oxide layer strengthening. We attribute the strengthening to two contributions: composite strengthening and strain gradient strengthening. The former is active from the beginning but gradually relaxes with oxide layer fracture. The latter contributes at the later stages of particle flattening when a highly deformed hard core is formed. These insights should prove useful specifically to understand bonding and consolidation mechanisms in solid-state powder-based processes.

# Declaration of competing interest

The authors declare that they have no known competing financial interests or personal relationships that could have appeared to influence the work reported in this paper.

#### Acknowledgment

MH and QT gratefully acknowledge the funding received by the National Science Foundation CAREER Award (CMMI-2145326). YI acknowledges funding received by JST PRESTO (Grant Number JPMJPR2091) and Japan Thermal Spray Society Research Grant Program (adopted in 2022).

#### Supplementary materials

Supplementary material associated with this article can be found, in the online version, at doi:10.1016/j.scriptamat.2024.116008.

### References

- [1] M. Hassani-Gangaraj, D. Veysset, V.K. Champagne, K.A. Nelson, C.A. Schuh, Adiabatic shear instability is not necessary for adhesion in cold spray, Acta Mater. 158 (2012) 429, 429
- [2] M. Hassani-Gangaraj, D. Veysset, K.A. Nelson, C.A. Schuh, In-situ observations of single micro-particle impact bonding, Scr. Mater. 145 (2018) 9–13.
- [3] L. He, D. Veysset, I.M. Nault, V.K. Champagne, M. Hassani, Impact and bonding behavior of core-shell powder particles, Surf. Coat. Technol. 441 (2022) 128591.
- [4] K. Ito, Y. Ichikawa, K. Ogawa, Experimental and numerical analyses on the deposition behavior of spherical aluminum particles in the cold-spray-emulated high-velocity impact process, Mater. Trans. 57 (2016) 525–532.
- [5] S. Zhou, J. Sun, C. Bernard, H. Lin, H. Saito, T. Miyazaki, Y. Ichikawa, K. Ogawa, Interfacial oxidation and boundary amorphization deposition mechanisms of GaN powder on metallic substrate by low-pressure cold spraying, Appl. Surf. Sci. 614 (2023) 156221.
- [6] H. Assadi, H. Kreye, F. Gärtner, T. Klassen, Cold spraying A materials perspective, Acta Mater. 116 (2016) 382–407.
- [7] T. Schmidt, F. Gärtner, H. Assadi, H. Kreye, Development of a generalized parameter window for cold spray deposition, Acta Mater. 54 (2006) 729–742.
- [8] T. Schmidt, H. Assadi, F. Gärtner, H. Richter, T. Stoltenhoff, H. Kreye, T. Klassen, From particle acceleration to impact and bonding in cold spraying, J. Therm. Spray Technol. 18 (2009) 794.
- [9] M. Hassani, V.K. Champagne, D. Helfritch, Bonding mechanisms in cold spray. Advances in Cold Spray, Elsevier, 2023, pp. 149–163.
- [10] A.A. Ward, C.A. Hareland, N.E. Palmerio, Z.C. Cordero, Thermally activated jamming in ultrasonic powder compaction, Adv. Eng. Mater. 23 (2021).
- [11] A.A. Ward, N.E. Palmerio, C.A. Hareland, Z.C. Cordero, Macroscopic yielding and particle-scale densification mechanisms in ultrasonic powder compaction, J. Mech. Phys. Solids. 167 (2022) 105011.
- [12] B. Chaudhary, N.K. Jain, J. Murugesan, Experimental investigation and parametric optimization of friction stir powder additive manufacturing process for aerospacegrade Al alloy, Int. J. Adv. Manuf. Technol. 123 (2022) 603–625.
- [13] A. Mukhopadhyay, P. Saha, Mechanical and microstructural characterization of aluminium powder deposit made by friction stir based additive manufacturing, J. Mater. Process. Technol. 281 (2020).
- [14] B. Chaudhary, M. Patel, N.K. Jain, J. Murugesan, V. Patel, Friction stir powder additive manufacturing of Al 6061/FeCoNi and Al 6061/Ni metal matrix composites: reinforcement distribution, microstructure, residual stresses, and mechanical properties. J. Mater. Process. Technol. 319 (2023) 118061.
- [15] J. Lienhard, C. Crook, M.Z. Azar, M. Hassani, D.R. Mumm, D. Veysset, D. Apelian, K.A. Nelson, V. Champagne, A. Nardi, C.A. Schuh, L. Valdevit, Surface oxide and

- hydroxide effects on aluminum microparticle impact bonding, Acta Mater. 197 (2020) 28–39.
- [16] Y. Ichikawa, K. Ogawa, Effect of substrate surface oxide film thickness on deposition behavior and deposition efficiency in the cold spray process, J. Therm. Spray Technol. 24 (2015) 1269–1276.
- [17] M. Hassani-Gangaraj, D. Veysset, K.A. Nelson, C.A. Schuh, Impact-bonding with aluminum, silver, and gold microparticles: toward understanding the role of native oxide layer, Appl. Surf. Sci. 476 (2019) 528–532.
- [18] W.-Y. Li, C.-J. Li, H. Liao, Significant influence of particle surface oxidation on deposition efficiency, interface microstructure and adhesive strength of coldsprayed copper coatings, Appl. Surf. Sci. 256 (2010) 4953–4958.
- [19] K.H. Ko, J.O. Choi, H. Lee, B.J. Lee, Influence of oxide chemistry of feedstock on cold sprayed Cu coatings, Powder. Technol. 218 (2012) 119–123.
- [20] M. Yu, W. Li, X. Guo, H. Liao, Impacting behavior of large oxidized copper particles in cold spraying, J. Therm. Spray Technol. 22 (2013) 433–440.
- [21] C.-J. Li, H.-T. Wang, Q. Zhang, G.-J. Yang, W.-Y. Li, H.L. Liao, Influence of spray materials and their surface oxidation on the critical velocity in cold spraying, J. Therm. Spray Technol. 19 (2010) 95–101.
- [22] K.H. Kim, W. Li, X. Guo, Detection of oxygen at the interface and its effect on strain, stress, and temperature at the interface between cold sprayed aluminum and steel substrate, Appl. Surf. Sci. 357 (2015) 1720–1726.
- [23] Y. Ichikawa, K. Shinoda, Current status and challenges for unified understanding of bonding mechanism in solid particle deposition process, Mater. Trans. 62 (2021) 691–702.
- [24] T. Nagae, M. Yokota, M. Nose, S. Tomida, T. Kamiya, S. Saji, Effects of pulse current on an aluminum powder oxide layer during pulse current pressure sintering, Mater. Trans. 43 (2002) 1390–1397.
- [25] G. Xie, O. Ohashi, M. Song, K. Furuya, T. Noda, Behavior of oxide film at the interface between particles in sintered Al powders by pulse electric-current sintering, Metallurg. Mater. Trans. A 34 (2003) 699–703.
- [26] P. Hendrickx, M.M. Tünçay, M. Brochu, Recyclability assessment of Al 7075 chips produced by cold comminution and consolidation using spark plasma sintering, Can. Metallurg. O. 55 (2016) 94–103.
- [27] Y.-W. Kim, W.M. Griffith, F.H. Froes, Surface oxides in P/M Aluminum a, JOM 37 (1985) 27–33.
- [28] X. Phung, J. Groza, E.A. Stach, L.N. Williams, S.B. Ritchey, Surface characterization of metal nanoparticles, Mater. Sci. Eng.: A 359 (2003) 261–268.
- [29] P.S. Grant, Spray forming, Prog. Mater. Sci. 39 (1995) 497-545.
- [30] Y. Li, Z. Zhang, R. Vogt, J.M. Schoenung, E.J. Lavernia, Boundaries and interfaces in ultrafine grain composites, Acta Mater. 59 (2011) 7206–7218.
- [31] S. Yin, X. Wang, W. Li, H. Liao, H. Jie, Deformation behavior of the oxide film on the surface of cold sprayed powder particle, Appl. Surf. Sci. 259 (2012) 294–300.
- [32] A. Navabi, M. Vandadi, T. Bond, V. Rahneshin, J. Obayemi, R. Ahmed, J. E. Oghenevweta, V. Champagne, N. Rahbar, W.O. Soboyejo, Deformation and cracking phenomena in cold sprayed 6061 Al alloy powders with nanoscale aluminum oxide films, Mater. Sci. Eng.: A 841 (2022) 143036.
- [33] W.-Y. Li, H. Liao, C.-J. Li, H.-S. Bang, C. Coddet, Numerical simulation of deformation behavior of Al particles impacting on Al substrate and effect of surface oxide films on interfacial bonding in cold spraying, Appl. Surf. Sci. 253 (2007) 5084–5091
- [34] S. Rahmati, R.G.A. Veiga, A. Zúñiga, B. Jodoin, A numerical approach to study the oxide layer effect on adhesion in cold spray, J. Therm. Spray Technol. 30 (2021) 1777–1791
- [35] H. Assadi, I. Irkhin, H. Gutzmann, F. Gärtner, M. Schulze, M. Villa Vidaller, T. Klassen, Determination of plastic constitutive properties of microparticles through single particle compression, Adv. Powder Technol. 26 (2015) 1544–1554.
- [36] G.E. Dieter, Mechanical Metallurgy, 3rd ed., McGraw-Hill, New York, 1961.
- [37] F.R.N. Nabarro, Z.S. Basinski, D.B. Holt, The plasticity of pure single crystals, Adv. Phys. 13 (1964) 193–323.
- [38] U.F. Kocks, The relation between polycrystal deformation and single-crystal deformation, Metallurg. Trans. 1 (1970) 1121–1143.
- [39] U.F. Kocks, Polyslip in single crystals, Acta Metallurg. 8 (1960) 345–352.
- [40] M. Liu, C. Lu, K.A. Tieu, C.-T. Peng, C. Kong, A combined experimental-numerical approach for determining mechanical properties of aluminum subjects to nanoindentation, Sci. Rep. 5 (2015) 15072.
- [41] Y. Kamimura, K. Edagawa, S. Takeuchi, Experimental evaluation of the Peierls stresses in a variety of crystals and their relation to the crystal structure, Acta Mater. 61 (2013) 294–309.
- [42] A. Cottrell, An Introduction to Metallurgy, CRC Press, 2019.
- [43] H. Koizumi, T. Koizumi, T. Kosugi, Determination of the pre-exponential factor and the activation energy for the low-temperature dislocation relaxation in aluminum, J. Alloys. Compd. 310 (2000) 107–110.
- [44] T. Kosugi, T. Kino, A new low-temperature dislocation-relaxation peak in aluminum, J. Phys. Soc. Jpn 58 (1989) 4269–4272.
- [45] N.-R. Kang, Y.-C. Kim, H. Jeon, S.K. Kim, J. Jang, H.N. Han, J.-Y. Kim, Wall-thickness-dependent strength of nanotubular ZnO, Sci. Rep. 7 (2017) 4327.
- [46] S. Hoffmann, F. Östlund, J. Michler, H.J. Fan, M. Zacharias, S.H. Christiansen, C. Ballif, Fracture strength and Young's modulus of ZnO nanowires, Nanotechnology 18 (2007) 205503.
- [47] I.C. Noyan, Plastic deformation of solid spheres, Philosoph. Mag. A 57 (1988) 127–141.

- [48] J. Paul, S. Romeis, J. Tomas, W. Peukert, A review of models for single particle compression and their application to silica microspheres, Adv. Powder Technol. 25 (2014) 136–153.
- [49] H.Z. Yu, M. Hassani-Gangaraj, Z. Du, C.L. Gan, C.A. Schuh, Granular shape memory ceramic packings, Acta Mater. 132 (2017) 455–466.
- [50] Y. Wang, Y. Zhu, Z. Yu, J. Zhao, Y. Wei, Hetero-zone boundary affected region: a primary microstructural factor controlling extra work hardening in heterostructure, Acta Mater. 241 (2022) 118395.